HAL
open science

Master/slave interferometry – ideal tool for coherence revival swept source optical coherence tomography

Adrian Bradu, Sylvain Rivet, Adrian Podoleanu

To cite this version:

Adrian Bradu, Sylvain Rivet, Adrian Podoleanu. Master/slave interferometry – ideal tool for coherence revival swept source optical coherence tomography. Biomedical optics express, 2016, 7 (7), pp.2453-2468. 10.1364/boe.7.002453 . hal-03700370

HAL Id: hal-03700370

https://hal.univ-brest.fr/hal-03700370

Submitted on 21 Jun 2022

HAL is a multi-disciplinary open access archive for the deposit and dissemination of scientific research documents, whether they are published or not. The documents may come from teaching and research institutions in France or abroad, or from public or private research centers.

L'archive ouverte pluridisciplinaire **HAL**, est destinée au dépôt et à la diffusion de documents scientifiques de niveau recherche, publiés ou non, émanant des établissements d'enseignement et de recherche français ou étrangers, des laboratoires publics ou privés.

Biomedical Optics EXPRESS

Master/slave interferometry – ideal tool for coherence revival swept source optical coherence tomography

Adrian Bradu,[1,*] Sylvain Rivet,[1,2] and Adrian Podoleanu[1]

[1]*Applied Optics Group, School of Physical Sciences, University of Kent, CT2 7NH Canterbury, UK*
[2]*Université de Bretagne Occidentale, EA 938 Laboratoire de Spectrométrie et Optique Laser, 6 avenue Le Gorgeu, C.S. 93837, 29238 Brest Cedex 3, France*
[*]*a.bradu@kent.ac.uk*

Abstract: In this paper, we demonstrate that the master slave (MS) interferometry method can significantly simplify the practice of coherence revival swept source optical coherence tomography (OCT) technique. Previous implementations of the coherence revival technique required considerable resources on dispersion compensation and data resampling. The total tolerance of the MS method to nonlinear tuning, to dispersion in the interferometer and to dispersion due to the laser cavity, makes the MS ideally suited to the practice of coherence revival. In addition, enhanced versatility is allowed by the MS method in displaying shorter axial range images than that determined by the digital sampling of the data. This brings an immediate improvement in the speed of displaying cross-sectional images at high rates without the need of extra hardware such as graphics processing units or field programmable gate arrays. The long axial range of the coherence revival regime is proven with images of the anterior segment of healthy human volunteers.

©2016 Optical Society of America

OCIS codes: (110.4500) Optical coherence tomography; (170.4460) Ophthalmic optics and devices; (120.3180) Interferometry; (200.4740) Optical processing.

References and links

1. W. Wieser, B. R. Biedermann, T. Klein, C. M. Eigenwillig, and R. Huber, "Multi-Megahertz OCT: High quality 3D imaging at 20 million A-scans and 4.5 GVoxels per second," Opt. Express **18**(14), 14685–14704 (2010).
2. T. Klein, W. Wieser, C. M. Eigenwillig, B. R. Biedermann, and R. Huber, "Megahertz OCT for ultrawide-field retinal imaging with a 1050 nm Fourier domain mode-locked laser," Opt. Express **19**(4), 3044–3062 (2011).
3. I. Grulkowski, J. J. Liu, B. Potsaid, V. Jayaraman, C. D. Lu, J. Jiang, A. E. Cable, J. S. Duker, and J. G. Fujimoto, "Retinal, anterior segment and full eye imaging using ultrahigh speed swept source OCT with vertical-cavity surface emitting lasers," Biomed. Opt. Express **3**(11), 2733–2751 (2012).
4. O. O. Ahsen, Y. K. Tao, B. M. Potsaid, Y. Sheikine, J. Jiang, I. Grulkowski, T.-H. Tsai, V. Jayaraman, M. F. Kraus, J. L. Connolly, J. Hornegger, A. Cable, and J. G. Fujimoto, "Swept source optical coherence microscopy using a 1310 nm VCSEL light source," Opt. Express **21**(15), 18021–18033 (2013).
5. M. Bonesi, M. P. Minneman, J. Ensher, B. Zabihian, H. Sattmann, P. Boschert, E. Hoover, R. A. Leitgeb, M. Crawford, and W. Drexler, "Akinetic all-semiconductor programmable swept-source at 1550 nm and 1310 nm with centimeters coherence length," Opt. Express **22**(3), 2632–2655 (2014).
6. D. D. John, C. B. Burgner, B. Potsaid, M. E. Robertson, B. K. Lee, W. J. Choi, A. E. Cable, J. G. Fujimoto, and V. Jayaraman, "Wideband Electrically-Pumped 1050 nm MEMS-Tunable VCSEL for Ophthalmic Imaging," J. Lightwave Technol. **33**(16), 3461–3468 (2015).
7. S. Yun, G. Tearney, J. de Boer, and B. Bouma, "Removing the depth-degeneracy in optical frequency domain imaging with frequency shifting," Opt. Express **12**(20), 4822–4828 (2004).
8. A. M. Davis, M. A. Choma, and J. A. Izatt, "Heterodyne swept-source optical coherence tomography for complete complex conjugate ambiguity removal," J. Biomed. Opt. **10**(6), 064005 (2005).
9. J. Zhang, J. S. Nelson, and Z. Chen, "Removal of a mirror image and enhancement of the signal-to-noise ratio in Fourier-domain optical coherence tomography using an electro-optic phase modulator," Opt. Lett. **30**(2), 147–149 (2005).
10. A. Bachmann, R. Leitgeb, and T. Lasser, "Heterodyne Fourier domain optical coherence tomography for full range probing with high axial resolution," Opt. Express **14**(4), 1487–1496 (2006).

#262003 Received 28 Mar 2016; revised 26 May 2016; accepted 26 May 2016; published 2 Jun 2016

11. Y. Yasuno, S. Makita, T. Endo, G. Aoki, M. Itoh, and T. Yatagai, "Simultaneous B-M-mode scanning method for real-time full-range Fourier domain optical coherence tomography," Appl. Opt. **45**(8), 1861–1865 (2006).
12. R. A. Leitgeb, R. Michaely, T. Lasser, and S. C. Sekhar, "Complex ambiguity-free Fourier domain optical coherence tomography through transverse scanning," Opt. Lett. **32**(23), 3453–3455 (2007).
13. R. K. Wang, "In vivo full range complex Fourier domain optical coherence tomography," Appl. Phys. Lett. **90**(5), 054103 (2007).
14. Y. K. Tao, M. Zhao, and J. A. Izatt, "High-speed complex conjugate resolved retinal spectral domain optical coherence tomography using sinusoidal phase modulation," Opt. Lett. **32**(20), 2918–2920 (2007).
15. H. Wang, Y. Pan, and A. M. Rollins, "Extending the effective imaging range of Fourier-domain optical coherence tomography using a fiber optic switch," Opt. Lett. **33**(22), 2632–2634 (2008).
16. B. Hofer, B. Povazay, B. Hermann, A. Unterhuber, G. Matz, and W. Drexler, "Dispersion encoded full range frequency domain optical coherence tomography," Opt. Express **17**(1), 7–24 (2009).
17. A. Bradu, L. Neagu, and A. Podoleanu, "Extra long imaging range swept source optical coherence tomography using re-circulation loops," Opt. Express **18**(24), 25361–25370 (2010).
18. A.-H. Dhalla, D. Nankivil, and J. A. Izatt, "Complex conjugate resolved heterodyne swept source optical coherence tomography using coherence revival," Biomed. Opt. Express **3**(3), 633–649 (2012).
19. A.-H. Dhalla, D. Nankivil, T. Bustamante, A. Kuo, and J. A. Izatt, "Simultaneous swept source optical coherence tomography of the anterior segment and retina using coherence revival," Opt. Lett. **37**(11), 1883–1885 (2012).
20. A. H. Dhalla, K. Shia, and J. A. Izatt, "Efficient sweep buffering in swept source optical coherence tomography using a fast optical switch," Biomed. Opt. Express **3**(12), 3054–3066 (2012).
21. D. Nankivil, A. H. Dhalla, N. Gahm, K. Shia, S. Farsiu, and J. A. Izatt, "Coherence revival multiplexed, buffered swept source optical coherence tomography: 400 kHz imaging with a 100 kHz source," Opt. Lett. **39**(13), 3740–3743 (2014).
22. Z. Hu and A. M. Rollins, "Fourier domain optical coherence tomography with a linear-in-wavenumber spectrometer," Opt. Lett. **32**(24), 3525–3527 (2007).
23. K. Gaigalas, L. Wang, H.-J. He, and P. DeRose, "Procedures for wavelength calibration and spectral response correction of CCD array spectrometers," J. Res. Natl. Inst. Stand. Technol. **114**(4), 215–228 (2009).
24. T.-H. Tsai, C. Zhou, D. C. Adler, and J. G. Fujimoto, "Frequency comb swept lasers," Opt. Express **17**(23), 21257–21270 (2009).
25. B. Liu, E. Azimi, and M. E. Brezinski, "True logarithmic amplification of frequency clock in SS-OCT for calibration," Biomed. Opt. Express **2**(6), 1769–1777 (2011).
26. Y. Yasuno, V. D. Madjarova, S. Makita, M. Akiba, A. Morosawa, C. Chong, T. Sakai, K.-P. Chan, M. Itoh, and T. Yatagai, "Three-dimensional and high-speed swept-source optical coherence tomography for in vivo investigation of human anterior eye segments," Opt. Express **13**(26), 10652–10664 (2005).
27. A. R. Tumlinson, B. Hofer, A. M. Winkler, B. Považay, W. Drexler, and J. K. Barton, "Inherent homogenous media dispersion compensation in frequency domain optical coherence tomography by accurate k-sampling," Appl. Opt. **47**(5), 687–693 (2008).
28. T. Hillman and D. Sampson, "The effect of water dispersion and absorption on axial resolution in ultrahigh-resolution optical coherence tomography," Opt. Express **13**(6), 1860–1874 (2005).
29. G. J. Tearney, B. E. Bouma, and J. G. Fujimoto, "High-speed phase- and group-delay scanning with a grating-based phase control delay line," Opt. Lett. **22**(23), 1811–1813 (1997).
30. S. Iyer, S. Coen, and F. Vanholsbeeck, "Dual-fiber stretcher as a tunable dispersion compensator for an all-fiber optical coherence tomography system," Opt. Lett. **34**(19), 2903–2905 (2009).
31. N. Lippok, S. Coen, P. Nielsen, and F. Vanholsbeeck, "Dispersion compensation in Fourier domain optical coherence tomography using the fractional Fourier transform," Opt. Express **20**(21), 23398–23413 (2012).
32. A. G. Podoleanu and A. Bradu, "Master-slave interferometry for parallel spectral domain interferometry sensing and versatile 3D optical coherence tomography," Opt. Express **21**(16), 19324–19338 (2013).
33. A. Bradu, M. Maria, and A. G. Podoleanu, "Demonstration of tolerance to dispersion of master/slave interferometry," Opt. Express **23**(11), 14148–14161 (2015).
34. A. Bradu, K. Kapinchev, F. Barnes, and A. Podoleanu, "On the possibility of producing true real-time retinal cross-sectional images using a graphics processing unit enhanced master-slave optical coherence tomography system," J. Biomed. Opt. **20**(7), 076008 (2015).
35. S. Rivet, M. Maria, A. Bradu, T. Feuchter, L. Leick, and A. Podoleanu, "Complex master slave interferometry," Opt. Express **24**(3), 2885–2904 (2016).
36. A. Bradu, K. Kapinchev, F. Barnes, and A. Podoleanu, "Master slave en-face OCT/SLO," Biomed. Opt. Express **6**(9), 3655–3669 (2015).

1. Introduction

Both implementations of spectral or Fourier domain optical coherence tomography (OCT), respectively spectrometer based (Sp) and swept source (SS), can be used to produce cross-sectional (B-scan) OCT images with high speed and high sensitivity. SS-OCT has some advantages over the Sp-OCT including a higher imaging speed [1,2], longer axial range and provides a quite uniform sensitivity over the axial range, which enables deeper structures to

#262003 Received 28 Mar 2016; revised 26 May 2016; accepted 26 May 2016; published 2 Jun 2016
(C) 2016 OSA

be visualized in a single scan. Although SS-OCT technology seems to win over Sp-OCT in most of the cases, there are applications that could benefit from an even more extended imaging range, such as the imaging of the ocular anterior segment or even of the entire human eye [3]. Unfortunately, due to the finite coherence length of the lasers used, the axial imaging range is still limited. An exception from this makes the new tunable vertical-cavity surface-emitting lasers (VCSEL) and akinetic light sources, which can provide a long axial range, exceeding 1 cm [4,5]. However, both VCSELs and akinetic light sources are only commercially available at longer wavelengths such as 1300 and 1550 nm and are more costly than the microelectromechanical system (MEMS) SSs widely available. To our knowledge, for shorter wavelengths, around 1050 nm, there are no SSs capable of providing extended (cm) axial ranges. Recently a new VCSEL light source in the 1050 range was demonstrated but of narrow tuning bandwidth [6].

As in all implementations of OCT, SS (MEMS, VCSEL, akinetic) and Sp-OCT the generation of images is based on a Fourier transform (FT), therefore mirror terms halve the achievable axial range. Numerous methods have been demonstrated to regain the full axial imaging range [7–17]. However, very often the improvements reported come at a price: reduced sensitivity, less axial resolution or speed, increased system complexity and associated cost, incomplete elimination of mirror terms, complex post-processing algorithms to be implemented, etc.

An elegant solution to increase the axial range in SS-OCT is the use of the coherence revival exhibited by some commercially available external cavity tunable laser (ECTL) swept sources [18]. The coherence revival method employs the interference between the waves reflected from the interferometer arms that originate from waves that suffered different multiple reflections inside the swept laser cavity. For the interference to occur, the difference between the optical path lengths of the interferometer arms are mismatched by an integer multiple of the roundtrip laser cavity length. This method is easy to implement, as only the optical path difference (OPD) between the two arms of the interferometer needs to be altered. As no additional hardware is required, the axial resolution is in principle not affected while the sensitivity drop is negligible.

The coherence revival technique shifts the maximum interference obtainable around OPD = 0 to values equal to multiples of the round trip in the laser cavity. The main difference is that while conventional OCT manifests no spectrum modulation at OPD = 0, coherence revival technique presents modulation around the OPD value where maximum of sensitivity is achieved. As explained in [18], the modulation is due to phase variations created by cavity length modulation during sweeping. Under coherence revival conditions, the channeled spectrum exhibits a different modulation density for positive and negative OPD values in the interferometer while the conventional OCT delivers the same modulation for the positive and negative OPD in the interferometer, equal in modulus (mirror terms). Therefore, the coherence revival technique offers a low cost solution for removal of mirror terms. Once this is achieved, an immediate advantage is doubling the axial range. In addition, working on OPD values of different multiplicities of the laser cavity length allows simultaneous imaging of samples at different distances from the system. An important such application is simultaneous imaging of the anterior and posterior segment of the eye [19]. Coherence revival is also applicable in conjunction with buffering methods to increase the sweeping of lasers with duty ratios below 50% [20,21].

However, there are some penalties in implementing the coherence revival via the conventional FT based method, as described below [18–21].

First, the k-clock equipping the ECTL swept source becomes unusable for correct data digitization, as the spectrum modulation is at least twice denser than in conventional operation. A new k-clock module needs to be re-built, or software methods of data resampling have to be employed instead [22–26]. The larger frequency clock needed leads either to an

#262003 Received 28 Mar 2016; revised 26 May 2016; accepted 26 May 2016; published 2 Jun 2016
(C) 2016 OSA

increase in the complexity of the imaging systems, hence to increased costs, or when data is resampled, to a reduction of the rate at which images are displayed.

Second, intensive dispersion compensation is required, as twice the laser cavity length is now within the total optical path difference creating the spectral modulation to be decoded by the digitizer. While for compensating for the dispersion in the interferometer both hardware optical methods and software (numerical) methods can be implemented [27–31], to compensate for the dispersion due to the laser cavity, only software solutions can be used. Normally, the implementation of any solution for dispersion compensation leads to an increase in the complexity of the systems or to heavy computation.

We demonstrate here, as an alternative to the FT based method, the utilization of the recently introduced Master/Slave (MS) OCT method in combination with the coherence revival technique, which eliminates the drawbacks specified above and allows real-time production of cross-sectional images. The MS method [32] is based on comparison of shapes of the channeled spectra at the interferometer output with stored channeled spectra shapes. An immediate advantage is that the MS technique can be implemented with raw data, without the need of organizing it in linear frequency slots (as required by conventional OCT technique, based on a FT). This means that no k-clock nor any resampling procedures are needed. Moreover, the MS method is immune to any dispersion left uncompensated within the optical path difference, which here includes the fiber in the laser cavity [33]. These two properties make the MS method an ideal tool for its combination with the coherence revival technique, offering the most simple and cost effective way to obtain extended axial range images without the need of data resampling or dispersion compensation.

In [34], real time production of cross-section MS-OCT images was made possible by using Graphics Processing Units (GPUs). Further progress in signal manipulation is reported here based on the simplified algorithm proposed in [35] that is incorporated here in a simple matrix multiplication. A second improvement is also based on the newest implementation of the MS method (Complex MS (CMS) [35]) that allows simplification of the preparation stage (Master). These improvements allow real-time display of processed B-scan MS-OCT images within the following frame without resorting to a GPU or a field programmable gate array, as previously reported [36].

2. Method

2.1 Strategies of producing reflectivity profiles in OCT

Let us refer comparatively to the two strategies of producing reflectivity profiles in OCT: FT based (conventional) and CMS based. Let us consider a continuum of values along the wavenumber coordinate *k*. To obtain the reflectivity profile, *A(z),* at a certain axial position (*z*) in the A-scan of the sample investigated, the integral of the product between the channeled spectrum $CS(\varphi_{k,z})$ from the sample and the kernel function e^{jkz} has to be calculated, where $\varphi_{k,z}$ is the phase of the measured channeled spectrum.

$$A(z)^{chirped} = \int_{-\infty}^{+\infty} CS(\varphi_{k,z}) \cdot e^{jkz} dk \tag{1}$$

Due to nonlinearities in the decoding procedure, from spectrum to time, typical for a real spectrometer or tuning swept source, the channeled spectrum is chirped. This means that the spectrum modulation does not exhibit a regular periodicity over the wavenumber axis. A second source of nonlinearity in wavenumber is that due to dispersion in the interferometer. Therefore, the phase is not directly proportional to *k*, but expressed in a general way as:

$$\varphi_{k,z} = g_k z + h_k \tag{2}$$

#262003 Received 28 Mar 2016; revised 26 May 2016; accepted 26 May 2016; published 2 Jun 2016
(C) 2016 OSA

The parameters g_k and h_k take into account the non-linear dependence of the phase on the wavenumber and on dispersion left unbalanced in the interferometer respectively [35]. These nonlinearities make the channeled spectrum chirped. To eliminate the effect of the chirping, two strategies can be employed:

2.1.1. Conventional FT based OCT

In this case, while the kernel function e^{jkz} is left untouched, each channeled spectrum is first resampled then multiplied with a function that cancels the effect of the dispersion to obtain a linear relationship between the phase of the modified channeled spectrum ($CS^{non\text{-}chirped}$) and k. As a result, a sufficiently accurate A-scan can be produced as a Fast Fourier Transform (FFT) of the $CS^{non\text{-}chirped}$:

$$A(z)^{non-chirped} = \int_{-\infty}^{+\infty} CS^{non-chirped}(k) \cdot e^{jkz} dk = FFT\left[CS^{non-chirped}(k)\right] \tag{3}$$

The advantage of this approach is the speed of the FFT. However, the preparatory steps to correct the data and produce $CS^{non\text{-}chirped}$ before performing FFT are computationally time expensive and prone to introducing errors. Moreover, the phase correction procedure has to be done for each acquired channeled spectrum, as illustrated in Fig. 1.

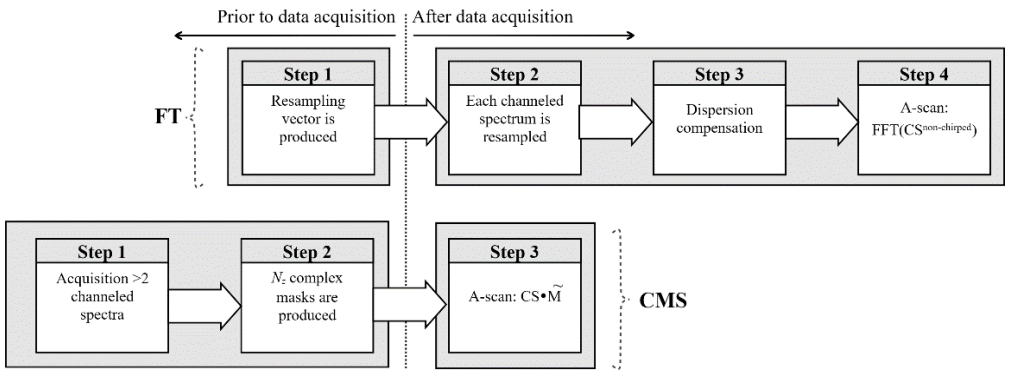

Fig. 1. Procedure steps required to produce an A-scan profile using the FT based OCT (top) and procedures steps to produce a single reflectivity value using the CMS method (bottom). The CMS-OCT method requires a single processing step after data acquisition while the conventional FT-OCT method is more time demanding, as three sequential steps are required.

2.1.2. MS based OCT

As the MS method is immune to the amount of unbalanced dispersion in the system or to the non-linearities of the spectra, its implementation is the same in both conventional and coherence revival based SS-OCT systems. The MS strategy consists in modifying the kernel function e^{jkz} in Eq. (1) rather than process the channeled spectra. In this case, to produce a single point in the A-scan, instead of a FFT, an integral of the product between the chirped channeled spectrum and a new kernel function $\tilde{M}(\varphi_{k,z})$ (denoted as complex masks) is performed [35]. As reflectivity of a single point only is delivered by such an integral calculation, the MS method may not present the speed advantage of the FFT; however, the MS method eliminates several disadvantages of the FFT method. The improved version of the MS-OCT recently reported, the CMS, allows calculation of complex masks $\tilde{M}(\varphi_{k.z})$ of components $\{M(\varphi_{1,z}), M(\varphi_{2,z}), \ldots M(\varphi_{N_k,z})\}$, with a component for each wavenumber pixel 1, 2,…N_k along the coordinate k. This procedure is documented in [35]. In order to obtain the reflectivity from an axial position z, it is sufficient to calculate:

#262003 Received 28 Mar 2016; revised 26 May 2016; accepted 26 May 2016; published 2 Jun 2016
(C) 2016 OSA

$$A(z)^{non-chirped} = \int_{-\infty}^{+\infty} CS(\varphi_{k,z}) \cdot \frac{\partial g}{\partial k} e^{j\varphi_{k,z}} dk = \int_{-\infty}^{+\infty} CS(\varphi_{k,z}) \cdot \tilde{M}(\varphi_{k,z}) dk \quad (4)$$

As illustrated in Fig. 1, the only step to be performed after data acquisition is the dot product between the recorded CS and the complex masks.

Obviously, when there is no nonlinearity in decoding the channeled spectrum, there is a linear distribution of frequencies along time ($g = k$), and if in addition $h = 0$ (no uncompensated dispersion), Eq. (4) is equivalent to Eq. (3).

2.2. Procedures of producing images in OCT

In the diagram shown in Fig. 1, the complete procedures of producing A-scans, using the FT-OCT (top) and CMS-OCT (bottom) are presented. Both techniques require a "calibration" step, before data acquisition, where the FT method entails three operations, which can only be executed sequentially whilst the CMS entails a single operation as described below.

2.2.1. Conventional FT based OCT

Let $k = 1 \ldots N_k$ be the number of wavenumber sampled points used to digitize each channeled spectrum, $z = 1 \ldots N_z$ the axial positions where the reflectivities are evaluated from and let $x = 1 \ldots N_x$ be the number of A-scans in each B-scan. An A-scan is produced as $FFT(CS_x^{\text{non-chirped}})$. Therefore, mathematically, a B-scan image can be described by:

$$B_{FFT} = \begin{bmatrix} FFT(CS_1^{\text{non-chirped}}) \\ FFT(CS_2^{\text{non-chirped}}) \\ \vdots \\ FFT(CS_{N_x}^{\text{non-chirped}}) \end{bmatrix} \quad (5)$$

where each of the components, $CS_x^{\text{non-chirped}}$, for $x = 1 .. N_x$, are resampled channeled spectra of N_k components each, recorded while scanning the beam over the sample. The size in pixels of the image thus obtained is $(N_x \times N_k)/2$ (N_x pixels laterally and $N_k/2$ pixels axially). To produce a cross-sectional image using conventional FTs:

1. A recalibration vector is produced (not required for swept sources equipped with k-clocks). This is a step performed prior to data acquisition.
2. The recalibration vector is used to resample each channeled spectrum via a spline cubic interpolation (not required for swept sources equipped with k-clocks). Obviously, this step takes place during or after data acquisition.
3. A procedure to compensate dispersion left unbalanced in the interferometer or/and dispersion due to the cavity when coherence revival is employed is needed. Again, this step can only take place during or after data acquisition.
4. A B-scan is produced by performing FFTs of the channeled spectra modified according to the steps 2 and 3 above.

The time required to produce a B-scan in FT based OCT includes the timing of sequentially executing the 3 last steps presented above. For swept sources equipped with k-clocks signals, the steps 1 and 2 can be eliminated, however due to difficulties to generate a clock signal when operating in the coherence revival regime, a k-clock may not be available.

2.2.2. MS based OCT

Numerically, Eq. (4) can be rewritten to describe the reflectivity value from a scattering center at an axial position *z,* by:

#262003 Received 28 Mar 2016; revised 26 May 2016; accepted 26 May 2016; published 2 Jun 2016
(C) 2016 OSA

$$A_z = \sum_{k=1}^{N_k} CS(\varphi_{k,z})\tilde{M}(k,z), \tag{6}$$

A B-scan image can be represented in a matrix form as:

$$B_{CMSI} = CS \times \tilde{M} \tag{7}$$

where CS, is a matrix of size $N_x \times N_k$, containing the channeled spectra CS_x, acquired for all lateral pixels $x = 1,2,\ldots N_x$ (along a laterally oriented scan), described by:

$$CS = \begin{bmatrix} CS_{11} & CS_{12} & \ldots & CS_{1N_x} \\ CS_{21} & CS_{22} & \ldots & CS_{2N_x} \\ \vdots & \vdots & \ddots & \vdots \\ CS_{N_k 1} & CS_{N_k 2} & \ldots & CS_{N_k N_x} \end{bmatrix} = \begin{bmatrix} CS_1 & CS_2 & \cdots & CS_{N_x} \end{bmatrix} \tag{8}$$

Each column of this matrix contains the N_k components of the channeled spectrum acquired for each lateral pixel, CS_x. Each of the components CS_{kx} is obtained after digitization. $\tilde{M}$ is a matrix of size $N_k \times N_z$, described by:

$$\tilde{M} = \begin{bmatrix} \tilde{M}_{11} & \tilde{M}_{12} & \ldots & \tilde{M}_{1N_k} \\ \tilde{M}_{21} & \tilde{M}_{22} & \ldots & \tilde{M}_{2N_k} \\ \vdots & \vdots & \ddots & \vdots \\ \tilde{M}_{N_z 1} & \tilde{M}_{N_z 2} & \ldots & \tilde{M}_{N_z N_k} \end{bmatrix} = \begin{bmatrix} \tilde{M}_1 \\ \tilde{M}_2 \\ \vdots \\ \tilde{M}_{N_z} \end{bmatrix} \tag{9}$$

Here, each row of the matrix $\tilde{M}$ is a complex signal of N_k components representing a mask produced for each axial position $z = 1,2,\ldots N_z$. The channeled spectra used in Eq. (4) to produce the B-scans, do not require any preparation, while the resulting B-scan images are completely free of eventual unbalanced dispersion or decoding nonlinearities.

A CMS based cross-sectional image is generated according to the following procedure:

1. With a high reflector as object, two or more experimental channeled spectra corresponding to different axial positions are stored. This step is performed only once for a given experimental set-up, before data acquisition.
2. The experimental channeled spectra recorded at the step above are then used to theoretically infer N_z complex masks (matrix $\tilde{M}$ in Eq. (9)), as described in [35]. This step, that is performed before data acquisition, needs to be repeated only if when the axial range displayed in the B-scan image is modified.
3. A cross-sectional image is produced by multiplying two matrices (Eq. (7). This step is performed as soon as raw data corresponding to a B-scan is acquired.

The size in pixels of the cross-sectional MS-OCT image produced in Eq. (7) is $N_x \times N_z$, different from that described by Eq. (5) for the FT case, which is $N_x \times N_k/2$. This axial range difference triggers a discussion on an important aspect: when using the conventional strategy, FFT based, the axial range of each A-scan scales from $z_{min} = 0$ to a maximum value z_{max}, determined by the sampling speed of the digitizer, hence by the number of sampling points N_k used to digitize the channeled spectrum. A modification of the axial range of interest (ROI), if needed, can only be achieved by effectively cropping the cross-section image, while a modification of the number of sampling points of the ROI is only possible by zero-padding the channeled spectra before FFT. In CMS, the axial length of the axial region of interest ROI is completely independent on the number of digitized points N_k. In addition, the axial range of interest as well as its coverage is adjustable by selecting the set of complex masks $\tilde{M}$ in terms of their axial position and increment between their depths.

#262003 Received 28 Mar 2016; revised 26 May 2016; accepted 26 May 2016; published 2 Jun 2016
(C) 2016 OSA

The time required to produce a CMS based B-scan image is given by the time to multiply two matrices. The FT based strategy is obviously faster in terms of producing a B-scan, when no data preparation is required before FFT. Indeed, in principle, for N_k points, a FFT based B-scan requires $N_x N_k \log_2 N_k$ operations, while a MS based B-scan obtained by matrix multiplication $N_x N_z(2N_k\text{-}1)$ operations. To obtain the same axial length image in both methods, $N_z = N_k/2$, in which case the FFT method is a clear winner. However, in practice the channeled spectra have to be prepared before FFT, i.e. data need to be organized in equal wavenumber slots that requires extra time and resources. In addition, images in the CMS-OCT, that use N_z less than $N_k/2$ can be quicker produced than using the FFT based OCT. For such cases, the time to produce B-scans via Eq. (7) is similar or shorter than the time required by FFT-OCT with resampling.

2.3 Experimental set-up

A schematic diagram of a coherence revival based SSOCT imaging system assembled for this study is depicted in Fig. 2. As optical source, a commercially available ECTL (Axsun Technologies, Billerica, MA) exhibiting coherence revival was employed. It has a central wavelength of 1060 nm, sweeping range 106 nm (quoted at 10 dB) and 100 kHz line rate. To ensure that the MS method can be employed, the stability of the source has been monitored over several months and concluded that its non-linearity function g_k does not show any fluctuations.

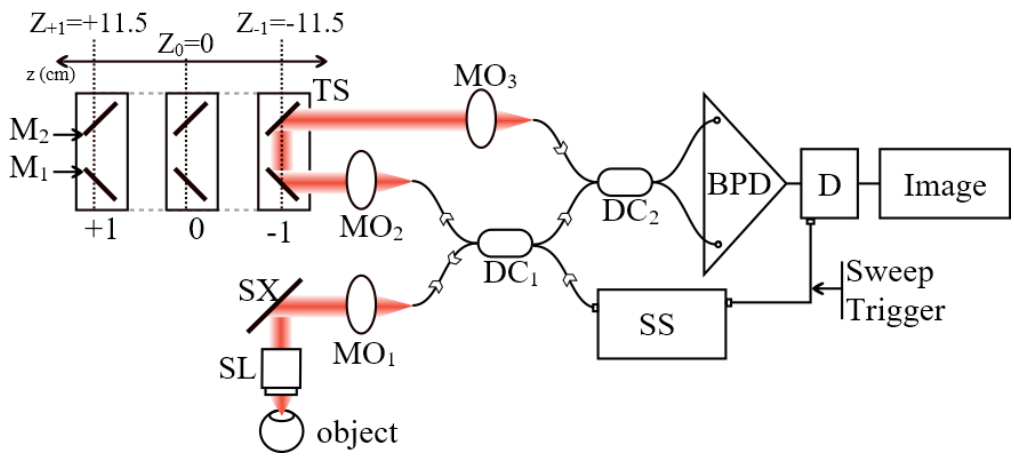

Fig. 2. Schematic diagram of the SS-OCT imaging system used in the present study. SS: swept source; DC1, DC2: directional couplers; BPD: balance photodetector; D: digitizer; $MO_{1\text{-}3}$: microscope objectives; TS: translation stage; $M_{1\text{-}2}$: flat mirrors; SX: transversal scanner; SL: scanning lens.

The interferometer configuration uses two single mode directional couplers, DC_1 and DC_2. DC_1 has a ratio of 20/80 and DC_2 is a balanced splitter, 50/50. DC_2 feeds a balance detection receiver BPD (Thorlabs, Newton, New Jersey, model PDB481C-AC), of 1 GHz electronic bandwidth. 20% from the SS power is conveyed towards the object arm, via a microscope objective MO_1 (focal length 15 mm), which collimates the beam towards a galvo-scanner SX, (Cambridge Technology, Bedford, MA, model 6110) followed by a scan lens SL (Thorlabs, model LSM04-BB). The power at the object is 1.9 mW. At the other output of DC_1, 80% from the SS power is directed towards the reference arm equipped with two flat mirrors, M1, M2, placed on a translation stage, TS to adjust the OPD in the interferometer. As TS, a linear actuator (Newport, Irvine, CA, model M-VP-25XA) was used, controlled by a Newport driver MM4005. Collimating microscope objectives MO_2 and MO_3 are identical to MO_1. The dispersion in the interferometer was left unbalanced, i.e. no glass slabs were used in the

#262003 Received 28 Mar 2016; revised 26 May 2016; accepted 26 May 2016; published 2 Jun 2016
(C) 2016 OSA

reference arm to compensate for the scan lens or other techniques were employed to compensate for the dispersion introduced by the laser cavity.

The signal from the BPD is sent to one of the two inputs of a dual input digitizer D (Alazartech, Quebec, Canada, model ATS9360). Data is digitized using the internal clock of the digitizer at 1GS/s, which leads to a maximum axial range of 12.4 mm. No data resampling procedures were implemented. Each channeled spectrum was digitized into N_k = 4096 sampling points. A number of N_x = 1000 channeled spectra were used to build each B-scan hence 10 ms acquisition per frame. The galvo-scanner is driven with a triangular waveform, where a half period of the driving signal is used to acquire data while during the second ramp, data is processed. Therefore, 20 ms are taken by each frame, hence the B-scan imaging proceeds at a 50 Hz rate. Sensitivity and fall-off measurements with an optical path difference of one cavity length were performed. The cavity length of the laser was measured by placing a mirror in the sample arm and adjusting the length of the reference arm. As in [17] we refer to order + 1 or −1 to the situations in which the sample arm was longer (Z_{+1} = + 11.5 cm) or shorter (Z_{-1} = −11.5 cm) than the reference arm by a laser cavity length, respectively and order 0 (Z_0 = 0) when the lengths of the two arms of the interferometer are equal.

3. Results and discussion

3.1 Sensitivity drop-off and axial resolution measurements

By altering the length of the reference arm, we found out that TS has to be moved by ± 11.5 cm between order 0 and + 1 or −1, as illustrated in Fig. 2, which corresponds to a length of around 80 mm of fiber. A similar cavity length was reported in [18].

In order to produce the complex masks $\tilde{M}_z$ (z = 1 ... N_z) a number of 5 channeled spectra corresponding to 5 different axial positions of the TS separated by 0.5 mm were acquired. We used the driver of the translation stage to control exact positioning with an error below 0.1 µm. However, we obtained similar results if the micrometer screw, with divisions at 5 µm was used, in which case the manual positioning is performed with an error below a couple of micrometers. Then:

(i) Using a simple linear regression of the first order derivative of the phase with respect to k, $\frac{\partial \varphi(k,z)}{\partial k}$, according to z, allows for removing the random noise and produces the parameters g_k and h_k [35].

(ii) Having the information about the non-linearity (g_k) and the amount of uncompensated dispersion (h_k), a digital format of Eq. (4) is used to produce the desired number of complex masks $\tilde{M}_z$. Then, Eq. (6) is employed to produce axial reflectivity profiles. The number of masks to be produced N_z, has to be large enough to ensure that the distance between consecutive points in the A-scan where the reflectivities are calculated at (digital axial resolution) is smaller than the axial optical resolution.

In Fig. 3, the sensitivity drop-off profile vs. the axial position $\delta z = z - Z_{+1}$ is shown (as the envelope of the signal for several measurements at different optical path differences, colored curves). This gives a full width at half maximum FWHM = 10 mm of the axial range. In addition, with the reference arm blocked, the axial confocal profile is shown (black curve), generated by measuring the DC signal at the photo-detector for different axial positions of a mirror as the object.

#262003 Received 28 Mar 2016; revised 26 May 2016; accepted 26 May 2016; published 2 Jun 2016
(C) 2016 OSA

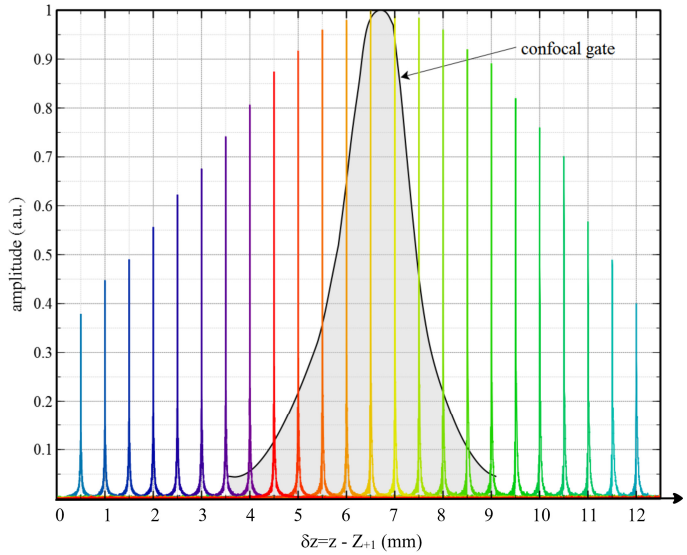

Fig. 3. Sensitivity fall-off measurements vs axial position δz, measured from Z_{+1} = 11.5 cm,, (colored) and the confocal profile (black).

The peak sensitivity is achieved at around δz = 6.0 mm, where the sensitivity reaches 101.3 dB (using the procedure detailed in [32]). The position δz = 6.0 mm determines an optical path difference between the arms of the interferometer equal to the roundtrip length of the laser cavity.

For δz_{min} = 0 mm, the channeled spectrum exhibits little modulation while for δz_{max} = 12.4 mm, a maximum modulation frequency of 500 MHz is obtained. The sensitivity drops by about 4 dB from the axial position where the peak sensitivity is measured to the edges of the axial range shown in Fig. 3 (δz_{min} = 0 mm and δz_{max} = 12.4 mm).

The long axial range of the coherence revival demands a low NA objective. It must be noticed that in practice, due to the need of good transversal resolution, the confocal gate determined by the MO_1 and the SL is usually narrower than the long axial range determined by δz_{max} and consequently the effective imaging range is lower than this value. According to the black curve presented in Fig. 3, the width of the confocal gate measured at $1/e^2$ from the maximum value is about 3.5 mm.

The procedure of producing the OCT sensitivity profiles is based on Eq. (6). This does not require any data resampling or numerical dispersion compensation, as the complex masks $\tilde{M}$ already incorporate the information on the chirp of the channeled spectra. The FWHM corresponding to the axial resolution of the system was measured for each sensitivity profile curve leading to a value of 6.85 ± 0.62 µm (where 0.62 is the standard deviation). In a conventional SS-OCT, to avoid degradation of the axial resolution, each channeled spectrum is subject to mathematical operations before performing FFT. After data resampling and numerically compensating for dispersion, an axial resolution of 6.96 ± 0.96 µm was found, which is similar to that obtained using the CMS technique.

3.2 Time benchmarking

To evaluate the conditions in which the CMS method can provide real-time cross-sectional images, we compared the time to produce a B-scan image using the CMS method with the time required to produce the same image via FFTs, when data was resampled only but not compensated for unbalanced dispersion. Our findings are summarized in Fig. 4.

#262003 Received 28 Mar 2016; revised 26 May 2016; accepted 26 May 2016; published 2 Jun 2016
(C) 2016 OSA

To perform the benchmarking, a LabVIEW 2015 (National Instruments, Austin Texas) project was created to run on a computer equipped with an Intel I7-5960X @ 3.0 GHz octacore processor (2 logical cores per physical core) and 16 GB of RAM.

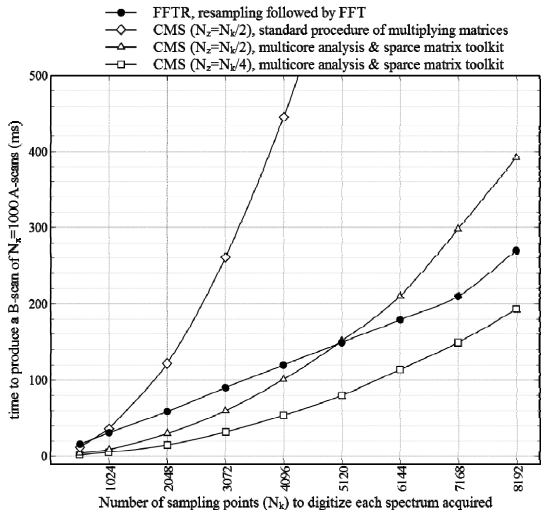

Fig. 4. Time to produce a cross-sectional image (B-scan) using both methods, FFT and CMS vs the number of sampling points used to digitize each channeled spectrum.

Each B-scan is built using N_x = 1000 A-scans. Two situations are considered for the CMS case, $N_z = N_k/2$ to mimic the axial size of the B-scan obtained in FFT based OCT and also a smaller number of sampled points, $N_z = N_k/4$. For the conventional case of resampled FFT method (FFTR) (solid circles in Fig. 4), data were resampled via a cubic B-spline interpolation procedure before FFT. The FFT requires $N_xN_k\log_2N_k$ operations. A fixed number of $N_z = N_k/2$ points was used axially. When using the CMS method, for the same number of $N_z = N_k/2$ axial points, a number of $N_xN_k(2N_k - 1)$ operations are required. Therefore, the time to produce a B-scan using the FFT approach (filled circles in Fig. 4) is shorter than the time to produce a CMS-OCT B-scan image (diamonds in Fig. 4). This curve was obtained using the standard procedure of multiplying matrices. Fortunately, high performance toolboxes that take advantage of the multicore design of the modern processors are already built within LabVIEW. By using the Multicore Analysis & Sparse Matrix toolkit (MASMT), the time performance of multiplying matrices is tremendously improved (triangles in Fig. 4). We have found that by using the same toolkit does not bring any improvement in speeding up the FFTs.

As it is demonstrated in Fig. 4, for small values of N_k, (up to around 5120 for the particular computer used in this study), the CMS technique with the adequate LabVIEW toolkit can produce B-scans faster than the procedure using the FFT after resampling (FFTR). Obviously, if data needed to be additionally compensated for dispersion, the FFT based method would have required even longer. By running our benchmarking project on computers with different, weaker CPU specifications, but with at least 4 cores, we found out that typically, CMS is faster than FFT when $N_k < 3000$. Typically, if the emphasis is not on a long axial range, there is no need for a high number of sampling points when digitizing data. For N_k = 4096 sampling points, with N_z = 2048 distinct points in depth, a B-scan can be produced in about 102 ms. This does not allow B-scans to be produced during the time of the next frame when using a 50-Hz galvo-scanner. However, such a performance is faster than the FFTR method (120 ms) but insufficiently quick to categorize the operation as truly real-time.

An exquisite capability of the MS method is the possibility to reduce the time to display the image by reducing the number of depth points, N_z. This number is not connected to N_k and

#262003 Received 28 Mar 2016; revised 26 May 2016; accepted 26 May 2016; published 2 Jun 2016
(C) 2016 OSA

by reducing N_z, the axial resolution is not affected, the image becomes sparse only. The drawback of this operation is either a reduction of the axial range (when N_z masks are produced to encode a shorter axial range than that determined by the digitizer) or a less axial resolution (when N_z less dense masks are produced to cover the full axial range determined by the digitizer). This limitation is not essential in most applications. For example, in our case, although it is possible to achieve an axial range as long as 12.4 mm, in practice this may not be as useful, as very often the axial range is limited by the extension of the confocal gate determined by the scan lens. With squares, we show in Fig. 4 that for a reduced number $N_z = N_k/4$ axial points in the A-scan (which corresponds to an axial range of around 6 mm if the density of masks is kept constant), the CMS technique can provide cross-sectional images faster than its FFTR counterpart for any number of sampling points N_k used to digitize the channeled spectra. According to the benchmarking shown in Fig. 4, for the particular case when $N_k = 4096$, and $N_z = N_k /4$, a B-scan image can be produced in 52 ms. This however is still insufficient to ensure real-time operation. Further benchmarking (not presented in Fig. 5) showed that for a 50-Hz galvo-scanner, real-time operation can be achieved when $N_z = N_k /10 = 409$, which corresponds to an axial range of around 2.4 mm if the density of masks is kept constant.

3.3 Imaging of the eye's anterior chamber

Figure 5 shows two images of a volunteer's ocular anterior segment. Both images were produced for the revival order +1, with maximum sensitivity set at $\delta z = 6$ mm. Each image, obtained by averaging five adjacent frames was obtained by keeping the length of the reference arm constant and moving the eye axially with respect to the scan lens. In this way, the effect of confocal gate on limiting the axial range is visible. Although our full axial range is around 12.4 mm with little decay in sensitivity from $\delta z_{min} = 0$ to $\delta z_{max} = 12.4$ mm, depending on the axial position of the eye, different parts of the anterior chamber are brightened up. The coherence revival images exhibit the property that the maximum sensitivity is in the middle of the image (and of the axial range), in comparison with conventional OCT images, where the maximum sensitivity is closer to zero optical path difference. In Fig. 5(a) the middle of the image coincides with the anterior chamber. In Fig. 5(b), we bring the crystalline lens closer to the middle of the axial range. Therefore, if in Fig. 5(a) the crystalline lens is hardly visible, it becomes a lot brighter in Fig. 5(b) where the corneal stroma is dimmer. The lateral resolution of the images experimentally measured using an USAF resolution test target is 19.7 µm.

To obtain Fig. 5, a number of $N_z = 2048$ masks (axial points) are used, hence a distance between consecutive masks (axial digital resolution) of about 5.85 µm. Laterally, each image comprises $N_x = 1000$ pixels, hence a lateral digital resolution of 14.5 µm. Both lateral and axial resolutions are measured in air.

#262003 Received 28 Mar 2016; revised 26 May 2016; accepted 26 May 2016; published 2 Jun 2016
(C) 2016 OSA

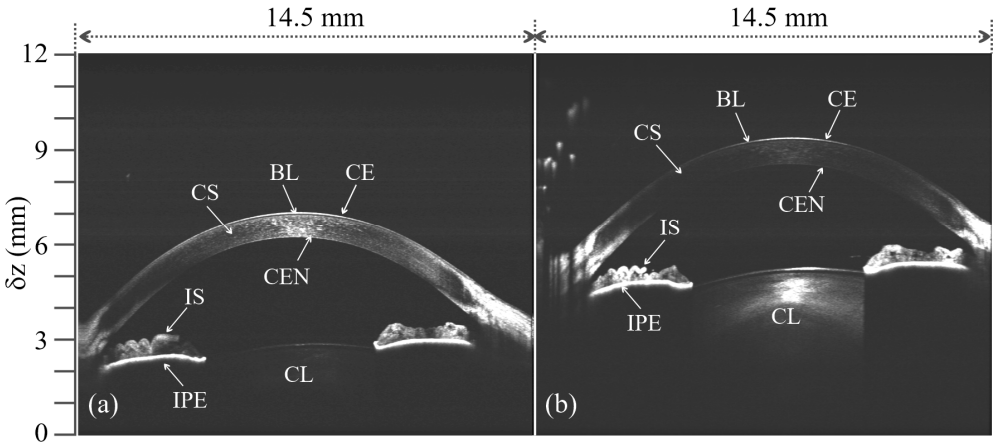

Fig. 5. Cross-sectional images of the ocular anterior segment of a healthy volunteer for 2 axial positions of the eye. Both images consist of N_x = 1000 lateral pixels and N_z = 2048 axial pixels. CE: corneal epithelium, BL: Bowman's layer, CS: corneal stroma, CEN: corneal endothelium, IS: iris stroma, IPE: iris pigment epithelium, CL: crystalline lens.

According to the benchmarking shown in Fig. 4, for N_k = 4096 and N_z = 2048 a B-scan can be produced in 100 ms, slightly faster than using the FT based OCT method. Consequently, the images in Fig. 5, covering an axial range of over 12 mm are produced at a frame rate of 10 Hz, however slower than the frame rate for real-time operation (50 Hz). When imaging the anterior chamber of the adult human eye, there is no need in principle for more than 6 mm axial range to image the entire segment from the corneal epithelium to the crystalline lens. Using the CMS, the axial range can be adjusted dynamically by simply restricting the axial range of the masks employed. In Fig. 6, a cross-sectional image of the anterior chamber spanning over 6 mm is shown. To produce it, the same number of $N_z = N_k /2$ = 2048 masks can be used, but corresponding to an axial range of 6 mm. This image was extracted from a movie (Visualization 1) produced still at 10 Hz as N_z = 2048.

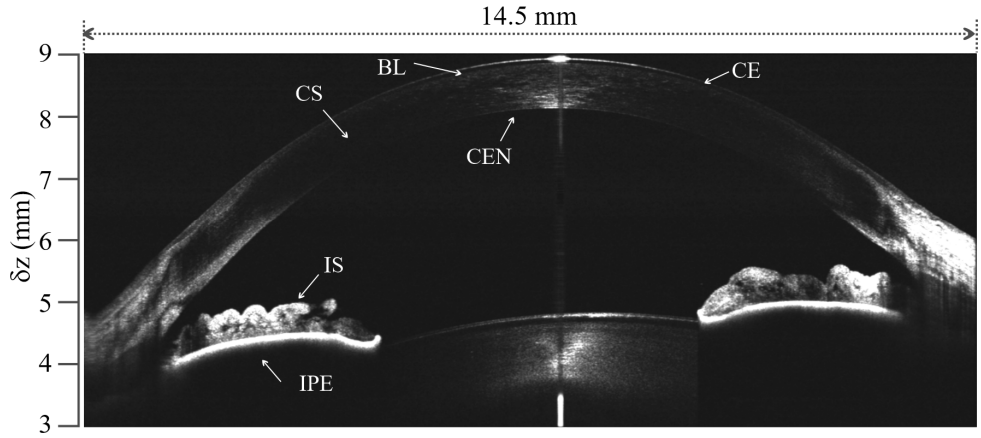

Fig. 6. Cross-sectional image of the ocular anterior segment of a healthy volunteer extracted from Visualization 1. The image consists of Nx = 1000 pixels laterally and Nz = 2048 pixels axially. CE: corneal epithelium, BL: Bowman's layer, CS: corneal stroma, CEN: corneal endothelium, IS: iris stroma, IPE: iris pigment epithelium, CL: crystalline lens.

For an axial range of 6 mm, the axial distance between two consecutive points, when N_z = 2048 in the A-scans is 2.92 µm, which is much better than the axial optical resolution of the

#262003 Received 28 Mar 2016; revised 26 May 2016; accepted 26 May 2016; published 2 Jun 2016
(C) 2016 OSA

system. To maintain the same digital axial resolution as in Fig. 5, the number of axial points N_z can be halved to 1024, in which case, each frame can be produced at around 20 Hz.

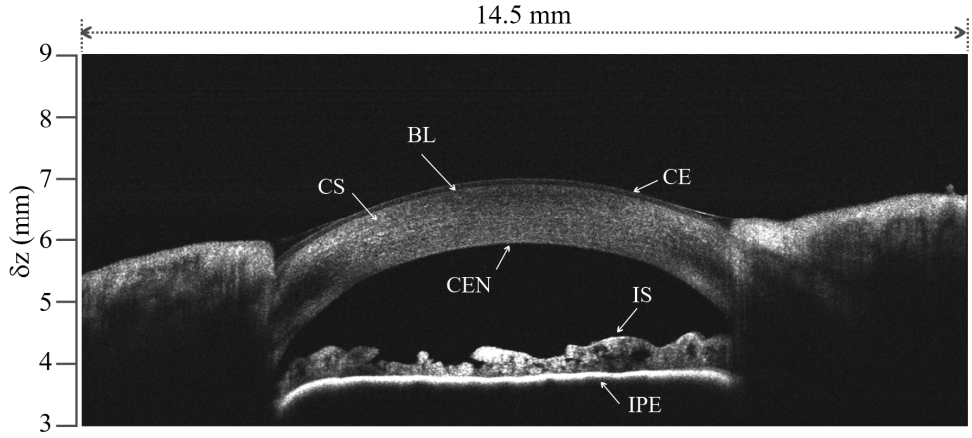

Fig. 7. Cross-sectional images of the ocular anterior segment of a healthy volunteer extracted from Visualization 2. The image consists of P = 1000 pixels laterally and R = 1024 pixels axially. CE: corneal epithelium, BL: Bowman's layer, CS: corneal stroma, CEN: corneal endothelium, IS: iris stroma, IPE: iris pigment epithelium, CL: crystalline lens.

As it can be seen in Fig. 7 (and Visualization 2), although axially only N_z = 1024 are used, the axial resolution is preserved, but the speed of producing the images improved by a factor of 2 while still producing mirror free long axial range images over an axial range with little sensitivity drop-off. Figure 7, is the first frame of a movie (Visualization 2, 20 Hz frame rate) produced while the laser beam was scanned over the whole anterior chamber.

4. Discussion and conclusion

We have demonstrated that CMS-OCT can be an ideal tool for coherence revival OCT imaging systems. The revival technique makes the production of long axial range, mirror term free cross-sectional images in OCT possible. The CMS technique simplifies it even further, as it eliminates the need of data resampling and the need for dispersion compensation, bringing speed to the production of OCT images.

The implementation of the CMS technique itself is simple. The calibration of the system (production of the masks) involves recording a few experimental channeled spectra only, process which has to be performed only once for any given set-up. For a calibrated set-up, high resolution, high sensitivity images are produced without the need of any sophisticated mathematical procedure: the only mathematical operation involved is the multiplication of two matrices. This is made possible by the CMS method. This is based on modifying the kernel function in Eq. (4) (that can be done at the Master stage) instead of modifying each channeled spectrum as required by the FT based method (operation that is done during the measurement stage).

As a result, there is no need to compensate for the large dispersion introduced by the laser cavity or for the dispersion due to unmatched optics and fiber lengths between the sample and reference arm of the interferometer. Equally, there is no need to resample data or build a new costly k-clock, which may be challenging due to the pronounced chirp and high density of peaks required to produce long axial range images. The artifacts reported in [18], at large frequencies, possible due to an imperfect resampling are not visible in any of the CMS images.

When used in conjunction with a coherence revival imaging system, the CMS method can provide images over the same long axial range as its FT based counterpart. However, due to its simpler implementation, CMS has the potential to produce images less affected by

#262003 Received 28 Mar 2016; revised 26 May 2016; accepted 26 May 2016; published 2 Jun 2016
(C) 2016 OSA

artefacts and also faster without resorting to extra hardware equipment. We have considered the option of harnessing the power of the GPUs, as the speed of performing matrix multiplications is superior to that of the CPU implementation. When harnessing the power of the GPUs, the speed of performing matrix multiplications is superior to that of the CPU implementation. However, irrespective of the GPU computing power, the repetitive process of data transfer to the shared memory accessible by the GPU program does not ensure a real time operation for large number of sampling points N_k [34], which is the case when the goal is to achieve a long axial range or a fast sweeping SS. This peculiarity would recommend utilization of field programmable gate arrays, however this implementation would be complex and costly.

In MS-OCT, to speed up the production of B-scans, it is possible to act on the size of the axial region of interest to be imaged. In FT-OCT, this range is determined by the speed of the digitizer that also determines the number of sampling points N_k to digitize each channeled spectrum.

The maximum axial range is determined in both methods, conventional FFT and MS by the number of sampling points N_k used to digitize each channeled spectrum. However, after acquisition, each method offers different functionality in preparing images. In FFT based OCT, the N_k number of points dictates the axial extension of the B-scan OCT image. A smaller region of interest (ROI) is achievable only by cropping the final image. In MS-OCT, the axial ROI is determined by N_z, the number of masks to be used at the Slave stage. Consequently, it is possible to adjust the ROI easily, to match the axial size of the sample to be imaged. A useful rule of thumb for producing high axial resolution images is to assemble axial reflectivities from consecutive points in the A-scan separated by no more than half of the axial optical resolution. In our case, as the axial resolution is around 7 µm, to produce a B-scan with a ROI of for example 2 mm, the reflectivity has to be estimated in only $N_z = 570$ points, instead of $N_k/2 = 2048$. The use of a large number of sampling points N_k for digitization cannot be avoided in a coherence revival system hence an increased computation time to resample data before FFT. MS-OCT solves this issue in an elegant way, by decoupling the axial ROI from N_k. In FFT based OCT, as the optical axial resolution is digitally compromised when an insufficient number of points is used to digitize the channeled spectra, very often data is zero-padded before FFT. In CMS, to tackle this inconvenient, a sufficiently large number N_z of axial reflectivities have to be estimated. For the images shown in the manuscript, we produced axial reflectivities from consecutive points (digital axial resolution) separated by 5.85 µm in Figs. 5 and 7, and 2.92 µm in Fig. 6 (to be compared with an optical axial resolution of 7 µm). Figures 5 and 7, although showing a lower digital axial resolution, provide either long axial range or speed. As in CMS, the axial ROI can be decoupled from N_k, the number of axial reflectivities N_z can be reduced up to the level where the digital resolution equals the optical one. In FFT based method, due to zero-padding the amount of data produced cannot be limited (to truncate the image axial range).

With a speed in displaying B-scans comparable or faster to those typically reported by FT-OCT systems, with tolerance to dispersion and elimination of the need to resample the data, as detailed here, MS-OCT can become the technique of choice for producing long axial range images via coherence revival not only in medical imaging but also in measuring long distances.

In fact, the adaptation of the MS technology to the coherence revival allows using the swept source on any of the multiples of the cavity length. This simplifies especially the assembly of adaptive optics configurations, where the arms are long and where such a method would allow performing OCT at any positions within a wide layout separated by 11.5 cm apart. There is no need of any extra procedure when changing the multiple order of laser cavity used, the only specific step is that of acquiring masks for each configuration used.

The MS method is an alternative to the FT based method, but better to be combined with the coherence revival technique, as it eliminates several important drawbacks associated to the

#262003 Received 28 Mar 2016; revised 26 May 2016; accepted 26 May 2016; published 2 Jun 2016
(C) 2016 OSA

FFT technique, as no need of zero-padding, re-sampling of data or dispersion compensation is required and allows real-time production of cross-sectional images.

Acknowledgments

A. Bradu and A. Podoleanu acknowledge the support of ERC (http://erc.europa.eu) COGATIMABIO 249889. S. Rivet acknowledges the Marie-Curie Intra-European Fellowship for Career Development, No. 625509. A. Podoleanu is also supported by the NIHR Biomedical Research Centre at Moorfields Eye Hospital NHS Foundation Trust and the UCL Institute of Ophthalmology, by the European Industrial Doctorate UBAPHODESA, FP7-PEOPLE-2013-ITN 607627 and by the Royal Society Wolfson Research Merit Award.